

Multilayer thin-film structures with high spatial dispersion

Martina Gerken and David A. B. Miller

We demonstrate how to design thin-film multilayer structures that separate multiple wavelength channels with a single stack by spatial dispersion, thus allowing compact manufacturable wavelength multiplexers and demultiplexers and possibly beam-steering or dispersion-control devices. We discuss four types of structure—periodic one-dimensional photonic crystal superprism structures, double-chirped structures exploiting wavelength-dependent penetration depth, coupled-cavity structures with dispersion that is due to stored energy, and numerically optimized nonperiodic structures utilizing a mixture of the other dispersion effects. We experimentally test the spatial dispersion of a 200-layer periodic structure and a 66-layer nonperiodic structure. Probably because of its greater design freedom, the nonperiodic structure can give both a linear shift with wavelength and a larger usable shift than the thicker periodic structure gives. © 2003 Optical Society of America
OCIS codes: 260.2030, 060.4230, 230.4170.

1. Introduction

Polychromatic light incident at an angle onto one of the surfaces of a prism is dispersed within the prism; i.e., light rays of different wavelengths propagate at different angles in the prism. Rays exiting the prism have a wavelength-dependent propagation angle that is due to the prism geometry.¹ Conventional prisms rely on material dispersion. Because the change in refractive index with wavelength is rather weak for transparent materials, the obtainable dispersion is limited. Previous research has shown that photonic crystal structures can be used to obtain much higher spatial dispersion.^{2–13} Photonic crystals are artificial structures composed of one-dimensional, two-dimensional, or three-dimensional periodic arrangements of different materials.¹⁴ Because of the wavelength-scale feature sizes of photonic crystals, these structures exhibit a behavior that is distinct from that of bulk materials. Wavelength regimes with high dispersion have been observed in theory and experiment for one-dimensional, two-dimensional, and three-dimensional photonic

crystals. As these artificial structures exhibit much higher dispersion than the material dispersion of conventional prisms, this phenomenon has been termed the superprism effect.

In this paper we investigate the superprism effect seen in one-dimensional thin-film structures. We concentrate on one-dimensional thin-film structures, as they can be easily and accurately fabricated with well-known deposition technology. This makes them interesting for commercial use and also for experimentally testing novel operation principles in well-controlled structures. Furthermore, these simpler structures also require less computation time during the design process, allowing for the numerical evaluation of a much higher number of different structures. Thin-film structures can readily be fabricated in nonperiodic sequences, which substantially and usefully increases the range of structures that can be investigated. As a future step, ideas resulting from one-dimensional structures can also be transferred to two- or three-dimensional structures, pointing at interesting directions of research.

In Section 2 we explore the superprism effect in a 100-period one-dimensional thin-film structure containing two dielectric layers per period. We operate the dielectric stack in reflection, performing two passes through the stack as depicted in the schematic in Fig. 1(a). Seen from the side, polychromatic light is incident from the top left corner onto the periodic dielectric stack. Just outside the stop band (the high-reflection spectral region), different wave-

The authors are with the Edward L. Ginzton Laboratory, Stanford University, Stanford, California 94305-4085. M. Gerken's e-mail address is gerken@stanford.edu.

Received 8 August 2002; revised manuscript received 6 November 2002.

0003-6935/03/071330-16\$15.00/0

© 2003 Optical Society of America

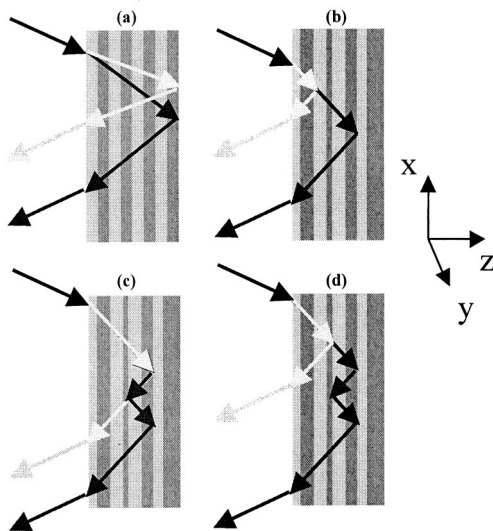


Fig. 1. Operating schematics of four types of thin-film structures that can be used for demultiplexing different wavelengths by spatial beam shifting. The structure in (a) is periodic, and those in (b)–(d) are nonperiodic. Polychromatic light is incident at an angle from the top left corner. All structures are operated in reflection and demultiplex light by a wavelength-dependent shift along the x axis. After exiting the structures, beams of different wavelengths propagate in parallel once again. For clarity, only two different wavelengths are pictured in the schematics. (a) The superprism effect for a one-dimensional photonic crystal (combined here with a simple reflection off the right face). Different wavelengths propagate at different group-velocity angles within the structure and are thus spatially shifted along the x axis. The nonperiodic structure in (b) reflects different wavelengths at different positions along the z axis. Because the structure is operated at an angle, this wavelength-dependent penetration depth leads to a spatial shift along the x axis. The structure in (c) exhibits wavelength-dependent stored energy. Stored energy is loosely equivalent to multiple bounces in the structure as indicated here. Again, because of the operation at an angle, beams of different wavelengths are shifted by different amounts along the x axis. Finally, the structure in (d) utilizes a combination of wavelength-dependent penetration depth and stored energy to demultiplex polychromatic light.

lengths propagate at different group-propagation angles within the thin-film structure. Therefore beams of different wavelengths exit the dielectric stack at different positions along the x direction. In connection with ultrafast optics, this effect has been called a spatial chirp.¹⁵ We experimentally observe this spatial shift with excellent agreement with theory. After exiting the dielectric stack, the beams propagate parallel once again. This research is an extension of our previous paper⁹ with improved structures and analysis.

For application purposes, it is desirable to have the ability to design the spatial dispersion with wavelength to given specifications. A linear spatial dispersion with wavelength or frequency is, for example, of practical interest for multiplexing or demultiplexing devices. Unfortunately, the design space of a periodic thin-film structure is very limited in that only the period length, the materials, the distribution

of the materials in a period, and the incidence angle can be chosen. Considering this limited number of degrees of freedom, it is not surprising that all periodic thin-film structures with two layers per period exhibit a similar nonlinear spatial shift with wavelength.

To achieve a linear spatial shift, we need to increase the degrees of freedom. One possible approach would be to increase the number of layers per period. For a sufficiently large number of periods, the optical properties within such a structure do not depend on the position in the structure, and the concept of effective optical properties is valid.^{3,4} Therefore increasing the number of layers per period is the method of choice if the application requires a constant phase velocity or group velocity within the volume of the structure, as, for example, for phase-matching purposes. For other applications, only the properties of the exiting light matter. In the case of a wavelength demultiplexer, for example, only the properties of the light along the exiting surface of the structure are important. As long as beams of different wavelengths are spatially separated at the exit surface, it does not matter what happened to the beams within the structure. This realization allows us to consider a whole new class of highly dispersive structures—nonperiodic structures with a high spatial dispersion along the exit surface. Nonperiodic structures have a much higher number of degrees of freedom. In addition to the materials and the incidence angle, we can choose all the layer thicknesses independently. With such a high number of degrees of freedom, we expect a much higher design freedom as well.

The difficult task is now to devise a design that fulfills the desired specifications, such as a linear shift with wavelength, and, ideally, to deduce design principles and physical understanding that permit future designs. Considering that a 200-layer structure has more than 200 degrees of freedom, searching the whole design space for an optimal structure is not a feasible solution. Although spatial dispersion of nonperiodic thin-film structures has not been investigated previously, several thin-film design methods have been developed for temporal dispersion-compensation purposes in femtosecond-laser cavities^{16–20} and optical fibers.^{21–23} In Section 3 we investigate the relationship between spatial and temporal dispersion and show that methods used for designing structures with temporal dispersion can be modified to obtain spatial dispersion.

In Sections 4 and 5 we investigate two new methods for obtaining spatial dispersion and how such structures can be devised using thin-film design techniques developed for temporal dispersion compensation. In Section 4 we explore nonperiodic thin-film structures that exhibit a wavelength-dependent penetration depth or turning point as schematically shown in Fig. 1(b). An example of such a structure is a chirped mirror, i.e., a dielectric stack with a position-dependent period length.^{16–18} Different wavelengths are reflected at different positions along

the z axis. Because the structure is operated at an angle, this wavelength-dependent penetration depth corresponds to a wavelength-dependent spatial shift along the x axis at the exit surface. Therefore such a structure can be used to demultiplex beams of different wavelengths by spatial beam shifting. In Section 5 we analyze structures that have a wavelength-dependent amount of stored energy. A simple example of this type of structure is a Fabry–Perot or Gires–Tournois resonator.²² These structures exhibit a large amount of stored energy for a resonant wavelength, whereas significantly less energy is stored off resonance. The stored energy effectively corresponds to multiple round trips in the cavity as indicated figuratively in Fig. 1(c). Again, because of the operation at an angle, beams of different wavelengths are shifted by different amounts along the x axis at the exit surface. Note that, in the case of stored energy, the beam shift can be larger than any that can occur for a single reflection inside the structure [as in Fig. 1(b)].

Both analytical design procedures discussed in Sections 4 and 5 are based on a reduction of the degrees of freedom to a smaller subset. For the design of a 200-layer structure, for example, not all possible 200-layer structures are considered, just a subset. We show that these methods can be used to design thin-film structures exhibiting a linear spatial shift along the x axis with wavelength. Furthermore, we investigate the limitations of these two analytical design procedures. In Section 6 we explain how the most general type of dispersive structure can be designed using numerical optimization techniques.^{24–29} In this procedure all the degrees of freedom are kept, and a locally optimal structure is achieved. We find that a dispersive thin-film structure obtained by numerical optimization combines effects based on a wavelength-dependent turning point with effects based on stored energy. We verify in theory and experiment that a linear shift with wavelength can be obtained using such a structure and that it is larger than can be obtained by a simple single reflection. Finally, we end with conclusions in Section 7.

2. Superprism Effect in One-Dimensional Photonic Crystals

Close to the stop-band edge, one-dimensional periodic structures exhibit a rapid change in the phase-velocity³ and group-velocity^{2,9} properties with wavelength. As we are here interested in the propagation direction of beams, we need to consider the group-propagation angle, which corresponds to the direction of energy flow.³⁰ Without a loss of generality, we can assume that the wave vector \mathbf{k} has components only in the x and z directions and is thus given by $\mathbf{k} = \beta\mathbf{x} + K\mathbf{z}$. For a periodic structure with a sufficient number of periods, the dispersion properties of the structure can be modeled by Bloch theory (see Appendix A).^{30,31} In this approach an infinite structure is assumed, and the dispersion relation among the wave vector K in the z direction, the wave vector β in the x direction, and the frequency ω is

obtained by use of periodic boundary conditions. The group velocity in the photonic crystal is given by Eq. (1), where the group velocities v_{gx} in the x direction and v_{gz} in the z direction are given by Eqs. (2) and (3)³⁰:

$$\mathbf{v}_g = \nabla_{\mathbf{k}}\omega(\mathbf{k}) = v_{gx}\mathbf{x} + v_{gz}\mathbf{z}, \quad (1)$$

$$v_{gx} = \left. \frac{\partial\omega}{\partial\beta} \right|_{K=\text{const}}, \quad (2)$$

$$v_{gz} = \left. \frac{\partial\omega}{\partial K} \right|_{\beta=\text{const}}. \quad (3)$$

The group-propagation angle θ_{gr} is calculated by use of Eq. (4):

$$\theta_{gr}(\omega, \beta, K) = \tan^{-1}(v_{gx}/v_{gz}). \quad (4)$$

All angles are taken with respect to the z axis. Thus θ_{gr} is 0° if the beam propagates along the z axis. In the case that K and β are given as functions of the frequency ω and the incidence angle θ , we can transform Eq. (4) into Eq. (5) by using a coordinate transformation and carefully calculating the partial derivatives:

$$\theta_{gr}(\theta, \omega) = \tan^{-1} \left[- \frac{\partial K(\theta, \omega)}{\partial \theta} / \frac{\partial \beta(\theta, \omega)}{\partial \theta} \right]. \quad (5)$$

This group-propagation angle is, of course, identical to the one obtained when we take the normal \mathbf{n} in a wave-vector diagram plotting contours of constant frequency^{2,9,30}:

$$\mathbf{n} = - \frac{\partial K(\theta, \omega)}{\partial \theta} \mathbf{x} + \frac{\partial \beta(\theta, \omega)}{\partial \theta} \mathbf{z}. \quad (6)$$

Finally, the exit position in reflection s_x along the surface of the dielectric stack in the x direction is given by Eq. (7), where θ_{gr} can be calculated with either Eq. (4) or (5):

$$s_x = 2L \tan(\theta_{gr}) = 2L(v_{gx}/v_{gz}). \quad (7)$$

In a bulk material the group-propagation angle θ_{gr} changes only slowly with wavelength. Therefore beams of different wavelengths exit the material at approximately the same position. Close to the stop band in a periodic dielectric stack, though, the group-propagation angle changes rapidly with wavelength. Owing to this superprism effect, beams of different wavelengths exit the material at different positions and are spatially demultiplexed.⁹ Figure 2 shows the theoretically calculated and experimentally verified shift with wavelength obtained by use of a 100-period dielectric stack.

The manufactured 100-period dielectric stack consists of 150-nm alternating layers of SiO_2 ($n = 1.456$ at 880 nm) and Ta_2O_5 ($n = 2.06$) with a total stack thickness of 30 μm on a quartz substrate ($n = 1.52$). A schematic of the experimental setup is shown in Fig. 3. Light of a tunable laser is focused onto the tilted sample under test. In a telescope-style setup

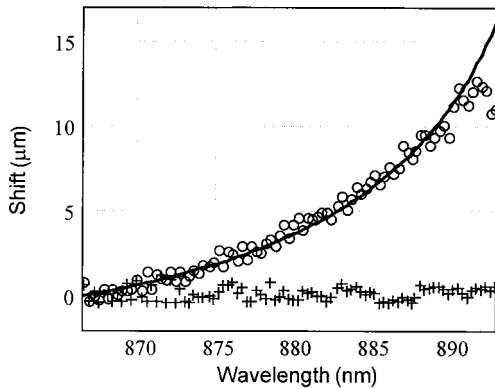


Fig. 2. Experimentally observed superprism effect for a 100-period dielectric stack for an incidence angle of 40° , p polarization, and a spot size of $4.7\ \mu\text{m}$. Two exiting beams are observed. The center positions of both beams are plotted as a function of wavelength. One beam (crosses) is reflected off the front of the dielectric stack owing to impedance mismatch and does not change position as a function of wavelength. The second beam (circles) is the real signal beam that propagates through the dielectric stack twice. This beam shifts as a function of wavelength. The solid curve shows the theoretically expected shift with wavelength calculated by use of Bloch theory.

the exiting light is focused onto a CCD camera. Owing to the light propagation through a tilted plate, the focal point in the plane of the light beams is different from the one perpendicular to the plane. The cylindrical lens compensates for this difference, such that both beam directions are focused on the CCD and the beam appears circular. The CCD trace is observed on the TV and oscilloscope as well as stored on a computer for further data evaluation. A tunable laser beam is incident on the dielectric stack through the substrate. For an incidence angle of 40° , p polarization, and a spot size of $4.7\ \mu\text{m}$, two exiting beams are observed (as well as a weak reflection off the air-substrate interface). One beam is caused by a reflection off the front of the dielectric stack owing to the impedance mismatch and does not change position as a function of wavelength. The intensity of this beam increases relative to the second beam as the reflectivity of the stack increases closer to the stop-band edge. The second beam is the real signal

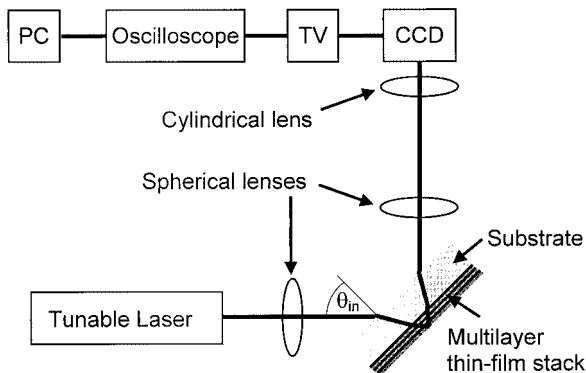


Fig. 3. Schematic of the experimental setup.

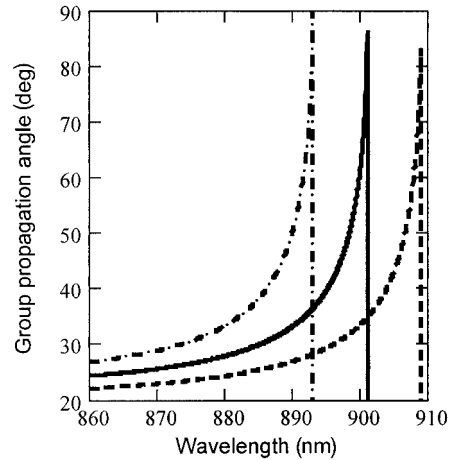


Fig. 4. Group-propagation angle as a function of wavelength calculated by use of Bloch theory with incidence angles of 40° (solid), 36.5° (dashed), and 43.5° (dash-dotted). For a Gaussian beam with a spot size of $4.7\ \mu\text{m}$ at $880\ \text{nm}$ and a center incidence angle of 40° , the intensity has decreased to $1/e^2$ for beam components at incidence angles of 36.5° and 43.5° .

beam that propagates through the dielectric stack twice as seen in Fig. 1(a). Figure 2 shows the center positions of the beams as a function of wavelength. The center positions are obtained by the fitting of the data to a Gaussian beam shape and adjustment of position, width, and amplitude. Excellent agreement between the experimentally observed shift and the theoretically expected shift along the x direction is obtained for the shifting beam.

The small spot size used in the experiment is necessary to prevent interference effects between the reflection off the front of the dielectric stack and the shifting beam. This small spot size also limits the maximum amount of shift observed in the experiment. Bloch theory predicts an increase of the spatial shift to the stop-band edge at $901\ \text{nm}$ with the group-propagation angle approaching 90° and the shift thus approaching infinity. In the experiment, however, we observe an increase in the shift only to around $892\ \text{nm}$. At larger wavelengths the beam appears quite distorted, and no clear peak can be determined. The reason for this discrepancy is that Bloch theory is exactly correct only for an infinitely wide beam as only one incidence angle is included in the calculation. All spatially limited beams have a larger angular content, corresponding to a range of incidence angles.³² For a Gaussian beam with a spot size of $4.7\ \mu\text{m}$ at $880\ \text{nm}$ and an incidence angle of 40° , the intensity has decreased to $1/e^2$ for beam components at incidence angles of 36.5° and 43.5° . As seen in Fig. 4, the stop-band edge is a function of the incidence angle. Therefore different parts of the beam are shifted by different amounts, leading to beam widening and distortion. These distortions limit the usable portion of the theoretically predicted shift and clarify why we observed a beam shift up to only $892\ \text{nm}$. At longer wavelengths, part of the beam is already within the stop band, distorting the

beam shape severely. This also explains why we will aim in the following sections for a linear shift with wavelength—for a linear shift with wavelength, the beam shape at the exit surface is independent of wavelength. Unfortunately, owing to the limited number of degrees of freedom available, a one-dimensional periodic dielectric stack with two layers per period cannot be designed to exhibit a linear shift with wavelength.

For the dispersive structure to be useful for applications, we furthermore need to eliminate the reflection off the front of the dielectric stack. This reflected beam is lost power, and, as we are operating close to the stop-band edge, this loss becomes significant. The reflection is due to an impedance mismatch between the substrate and the periodic dielectric stack that is caused mainly by the sudden periodicity and not as much by the difference in refractive index.¹⁹ The same problem occurs in corrugated waveguide structures and in fiber Bragg gratings. In the case of corrugated waveguides, the reflection can be eliminated by a tapering of the surface relief,² whereas in the case of apodized fiber Bragg gratings, the refractive-index contrast is slowly increased.^{33,34} To prevent the reflection off the front of the thin-film stack, we could use a tapered Bragg stack.¹⁹ In such a Bragg stack the periodicity is slowly turned on when the amount of high-index material in each period is increased. In Sections 4–6 we will discuss the design of thin-film structures that have a linear shift with wavelength and are impedance matched to prevent loss.

3. Relationship between Spatial and Temporal Dispersion

In this section we will explore the relationship between spatial and temporal dispersion characteristics and justify why design methods used for structures with temporal dispersion can also be applied in the case of spatial dispersion. Spatial dispersion manifests itself in a change of the beam exit position s as a function of wavelength. Temporal dispersion refers to the change in the group delay τ_{group} upon reflection as a function of wavelength. The group delay is calculated when the shift s along the x direction is divided by the speed of light v_{gx} in this direction. As shown in Eq. (8), we can rewrite this expression in terms of the more commonly used dependence on the phase upon reflection $\phi_{\text{refl}} = 2LK$ using Eq. (7):

$$\begin{aligned}\tau_{\text{group}} &= \frac{s}{v_{gx}} = s \left. \frac{\partial \beta}{\partial \omega} \right|_{K=\text{const}} \\ &= 2L \left. \frac{\partial K}{\partial \omega} \right|_{\beta=\text{const}} = \left. \frac{\partial \phi_{\text{refl}}}{\partial \omega} \right|_{\beta=\text{const}}.\end{aligned}\quad (8)$$

In the case of a periodic structure, the relationship among the wave vector K in the z direction, the wave vector β in the x direction, and the frequency ω is obtained from Bloch theory as shown in Appendix A. For a nonperiodic structure, we can use a standard

transfer-matrix technique to relate K , β , and ω . This is demonstrated in Appendix B. Calculations on test structures show that the group velocity v_{gx} is approximately constant with wavelength, and the group delay is thus proportional to the spatial shift. This result is not completely surprising, as v_{gx} is the group velocity along the layers. In Appendix C we prove that within a WKB-type approximation the spatial shift and the group delay are exactly proportional, as v_{gx} is independent of wavelength. This result provides physical insight and has practical consequences. As spatial and temporal dispersion are approximately proportional, existing structures with temporal dispersion can be modified to obtain structures with spatial dispersion. This is demonstrated in the next two sections. Furthermore, we see that a spatial shift with wavelength corresponds at the same time to a temporal delay. If a temporal delay is not desired, two structures with opposite spatial dispersions can be used in series. With the correct arrangement, this doubles the spatial shift and removes the temporal delay between wavelengths. If, however, the temporal delay is desired, the light could be backreflected through the same structure, canceling the spatial shift and doubling the temporal delay.

4. Dispersion Due to a Wavelength-Dependent Penetration Depth

Temporal dispersion compensation plays an important role in femtosecond lasers. Double-chirped mirrors are well suited for femtosecond-laser cavities as they have a broad bandwidth and can, at the same time, be used to compensate for temporal dispersion.¹⁹ In a Bragg mirror, light is strongly reflected only for wavelengths near the Bragg wavelength. In a simple-chirped mirror, the Bragg wavelength is slowly changed as a function of the position in the stack. If the increases in the period length come from the incidence side, longer wavelengths penetrate deeper into the structure and thus accumulate more delay upon reflection. For the opposite chirp, shorter wavelengths penetrate deeper, and the opposite dispersion is obtained. As mentioned in Section 3, the sudden turn-on of the periodicity leads to a reflection off the front of the dielectric stack. The second chirp achieves impedance matching and prevents this reflection. An analytical design of such mirrors is possible by use of an exact coupled-mode theory¹⁸ and a WKB-type approximation.²⁰

Remember that temporal dispersion and spatial dispersion are approximately proportional, and therefore that same algorithm can be used to design a structure with spatial dispersion. First, a structure with temporal dispersion is designed as described in Ref. 20. A standard Bragg reflector may follow the double-chirped mirror section to increase the reflectivity to unity. This normal-incidence design is then modified for oblique incidence by our taking into account that the Bragg wavelength λ_B is given by Eq. (9), where n_H and n_L are the refractive indices; d_H and d_L are the thicknesses of the high-

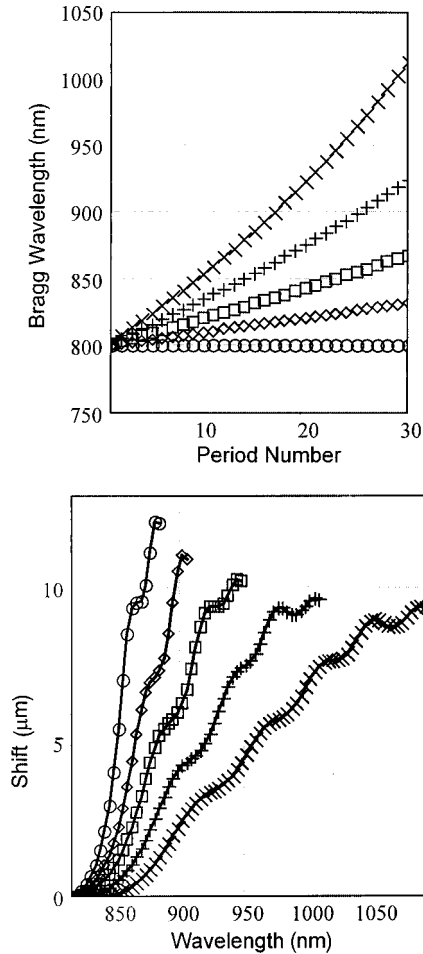


Fig. 5. (a) Bragg wavelength as a function of the position in the structure for five different 60-layer $\text{SiO}_2\text{-Ta}_2\text{O}_5$ double-chirped mirror designs. Layer data represented as follows: $f = 0.5$ (exes), $f = 0.33$ (crosses), $f = 0.2$ (squares), $f = 0.1$ (diamonds), $f = 0$ (circles). (b) The theoretical spatial shift as a function of wavelength is plotted for an incidence angle of 45° and p -polarized light. An approximately linear shift is observed for all five designs. The dispersion increases with decreasing chirp in the Bragg wavelength. The maximum dispersion is achieved with a single-chirped Bragg stack (circles).

and low-index materials, respectively; and θ is the incidence angle in vacuum:

$$\lambda_B = 2 \left(n_H d_H \left\{ 1 - \left[\frac{\sin(\theta)}{n_H} \right]^2 \right\}^{1/2} + n_L d_L \left\{ 1 - \left[\frac{\sin(\theta)}{n_L} \right]^2 \right\}^{1/2} \right). \quad (9)$$

Figure 5 compares the performance of five different 60-layer structures designed in this manner. Figure 5(a) shows the chirped Bragg wavelength as a function of the period number p calculated by use of Eq. (10) and five different factors f :

$$\lambda_B(p) = \frac{800 \text{ nm}}{\sqrt{1 - 0.02541 fp}}. \quad (10)$$

By use of this chirped Bragg wavelength, the layer thicknesses of the single-chirped structures are calculated with Eqs. (11) and (12):

$$d_{HSC}(p) = \frac{\lambda_B(p)}{4n_H \left\{ 1 - \left[\frac{\sin(\theta)}{n_H} \right]^2 \right\}^{1/2}}, \quad (11)$$

$$d_{LSC}(p) = \frac{\lambda_B(p)}{4n_L \left\{ 1 - \left[\frac{\sin(\theta)}{n_L} \right]^2 \right\}^{1/2}}. \quad (12)$$

To achieve impedance matching, the first P_{DC} periods are double chirped as given in Eqs. (13) and (14):

$$d_{HDC}(p) = \frac{\lambda_B(P_{DC})}{4n_H \left\{ 1 - \left[\frac{\sin(\theta)}{n_H} \right]^2 \right\}^{1/2}} \left(\frac{p}{P_{DC}} \right)^{1.05}, \quad (13)$$

$$d_{LDC}(p) = \frac{\frac{\lambda_B(p)}{2} - d_{HDC}(p)n_H \left\{ 1 - \left[\frac{\sin(\theta)}{n_H} \right]^2 \right\}^{1/2}}{4n_L \left\{ 1 - \left[\frac{\sin(\theta)}{n_L} \right]^2 \right\}^{1/2}}. \quad (14)$$

In our calculations, 25 of the 30 periods are double chirped.

In Fig. 5(b) the spatial shifts as a function of wavelength are plotted for the five designed structures. For clarity the shift is plotted only up to the wavelength at which it stops increasing. We see that all five structures have an approximately linear shift with wavelength as desired. Structures with a larger chirp in the Bragg wavelength exhibit less dispersion but show that dispersion over a larger wavelength range. The maximum shift is approximately constant for the given allowed ripple. There is a trade-off between the maximum shift and the ripple³⁵ in the shift for a given number of layers. That is, we could design a structure with less ripple and less shift or a structure with more ripple and more shift, depending on the application requirements. As the dispersion increases with decreasing chirp in the Bragg wavelength, the maximum dispersion is achieved with a simple Bragg stack (though the ratio between high- and low-index material in a period is still chirped for impedance matching). Note that this linear shift appears within the stop band of the single-chirped Bragg stack. It is not identical to the nonlinear shift observed just outside the stop band as discussed in Section 2. The double-chirped mirror design algorithm cannot be used to obtain a higher dispersion for the given number of layers. This limitation of the dispersion is not a fundamental physical limit for layered dielectric structures. As we will see in Section 5, structures with larger dispersion can be designed. Rather, the limitation is due to the fact that in this algorithm the degrees of freedom are limited, and only a subset of all possible structures is considered. Specifically,

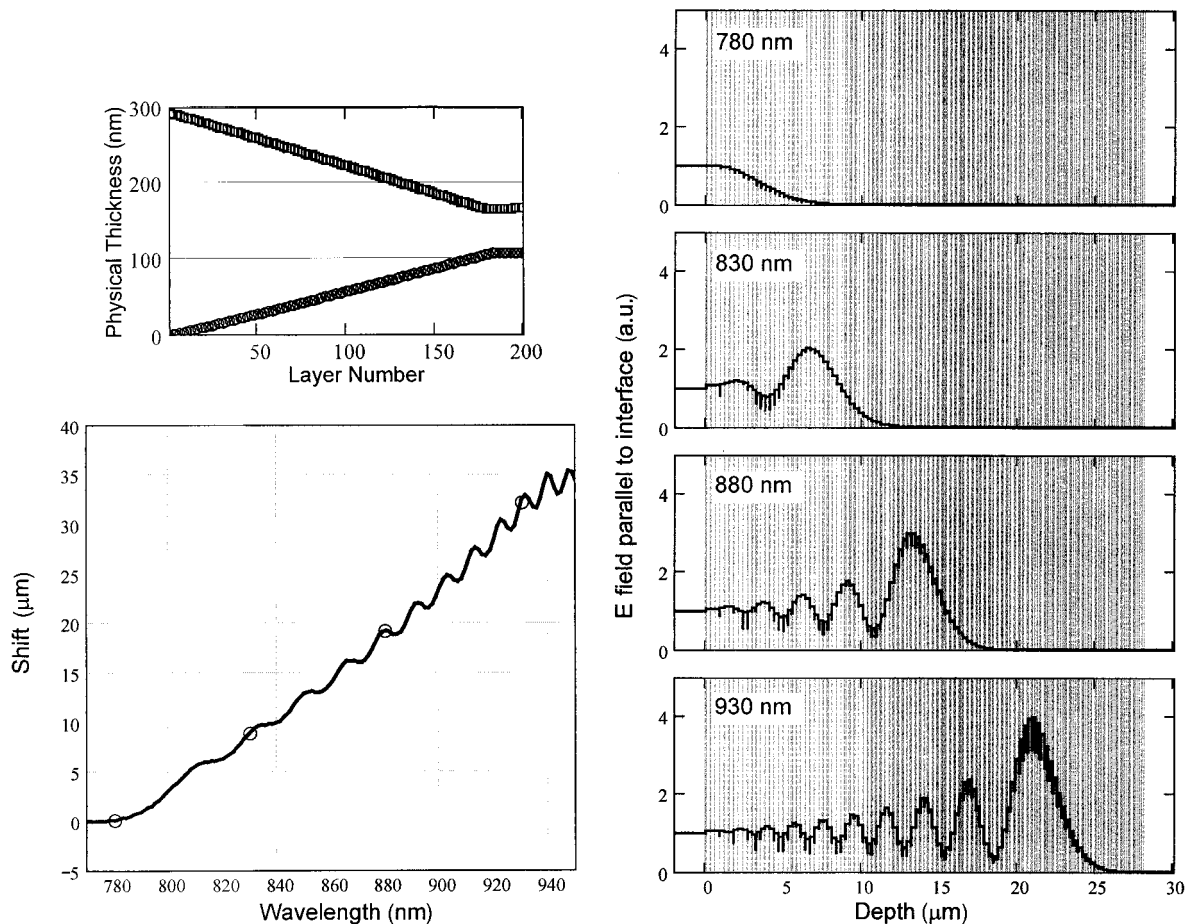


Fig. 6. (a) Physical layer thicknesses for a 200-layer $\text{SiO}_2\text{-Ta}_2\text{O}_5$ double-chirped structure. Layer data represented as follows: SiO_2 [squares] and Ta_2O_5 (circles). (b) Theoretically calculated shift as a function of wavelength at a 40° incidence angle and p polarization. (c) E fields parallel to the interfaces of the forward-propagating waves as a function of the position in the structure for four wavelengths—780, 830, 880, and 930 nm. The vertical lines indicate the position of the interfaces between layers. Light is incident from the left, and the structure extends from 0 to $28\text{ }\mu\text{m}$. It can clearly be seen that light of longer wavelengths penetrates deeper into the structure, leading to temporal and spatial dispersions. Furthermore, the larger-than-unity field amplitudes for the longer wavelengths indicate additional dispersion that is due to stored energy.

the algorithm allows only for a monotonic change in the Bragg wavelength. We can easily imagine that releasing this requirement would allow for other structures that might have a larger dispersion.

The calculations in Fig. 5 are done with the transfer-matrix method given in Appendix B applied to the center ray of the beam. This plane-wave approximation correctly predicts the behavior of a Gaussian beam if the shift does not exhibit any rapid changes with wavelength. Rapid oscillations in the shift are indicative of interference effects between different beams. An example is the periodic structure discussed in Section 2. The plane-wave approximation predicts strong oscillations in the shift with wavelength, but, with sufficient focusing, we actually see two separate beams—one that is stationary, corresponding to a reflection off the front of the stack, and one that changes position with wavelength. These distinct beams cannot be predicted by the plane-wave approximation, and the full beam behavior has to be modeled. For the double-chirped struc-

tures discussed in this section, however, the plane-wave approximation can be used as all reflections, except the desired shifted beam, are suppressed sufficiently well, and no rapid changes appear in the dispersion. In particular, the reflection off the entering side of the structure has been suppressed by the impedance-matching chirp.

To visualize the origins of dispersion, we plot the E-field amplitude of the forward-propagating wave as a function of the position in the structure. Because the structures we are discussing here are nearly 100% reflecting, the amplitudes of the forward- and backward-propagating waves are nearly equal for any specific wavelength. Interference effects between the forward- and backward-propagating waves form a rapidly oscillating standing-wave pattern. The amplitude of the forward-propagating wave outlines the envelope of this standing-wave pattern. Figure 6(a) shows an example of a 200-layer double-chirped structure. In Fig. 6(b) we see, as expected, that the field penetrates deeper into the structure

with increasing wavelength, resulting in both temporal and spatial dispersion. Interestingly, the total observed shift of 35 μm exceeds the maximum shift of 25 μm expected for a beam propagating all the way through the 28- μm structure with an average refractive index of 1.6 and back. Thus the structure exhibits additional dispersion that cannot be explained by the penetration depth. This extra dispersion is due to stored energy. In Fig. 6(c), larger-than-unity E-field amplitudes correspond to energy buildup. We observe that only the shortest wavelength plot does not exhibit any energy buildup. For the other wavelengths, the field forms an Airy-type standing-wave pattern, as is usual for a linearly changing potential. As will be explained in greater detail in Section 5, stored energy results in dispersion, thus explaining the larger-than-expected total shift in Fig. 6(b). Note also that this structure stores energy without the use of a front mirror; rather, energy is stored solely owing to the shape of the potential. In other words, the structure stores energy without requiring a resonant cavity in the conventional sense. The position of the energy buildup changes continuously with wavelength. This effect might be interesting for future active and passive devices.

In conclusion, we demonstrated in this section that structures with a wavelength-dependent penetration depth exhibit spatial dispersion. An analytical design method based on a WKB-type approximation can be used to obtain structures with a monotonically increasing or decreasing shift with wavelength.²⁰ This method is useful for broadband designs with rather low dispersion, but it is not suitable for designing structures with high dispersion. In Section 5 we will examine a different design method that is particularly useful for narrowband designs with high dispersion.

5. Dispersion Due to Stored Energy

In this section we investigate structures with dispersion that is due to a wavelength-dependent amount of stored energy. Simple examples of this type of structure are Fabry–Perot and Gires–Tournois resonators.^{15,21,22,26} A Fabry–Perot structure consists of a cavity between two partial reflectors. At the resonant wavelength the transmittance of the filter is unity, and a maximum amount of energy is stored in the cavity. A Gires–Tournois structure consists of one partial reflector, a cavity, and a 100% reflector. For this resonator the reflectance is unity at all wavelengths, though, again, the amount of stored energy is maximum at the resonant wavelength. As one moves from the resonant wavelength, the amount of stored energy decreases. Because the amount of stored energy is related to the effective number of round trips in the cavity, these resonator structures exhibit spatial dispersion as schematically depicted in Fig. 1(c). The transmittance and reflectance for the respective structures are unity only in the absence of absorption. For structures with absorption, the loss is highest at the resonant wavelength because the beam executes the maximum number of

round trips. Resonators allow for high dispersion over a narrow wavelength range. Unfortunately, the degrees of freedom in the design of a single-cavity resonator structure are very limited. For example, in the case of the Gires–Tournois structure we can choose only the reflectivity of the partial reflector and the cavity thickness. Not surprisingly, the shape of the dispersion is quite similar for all Gires–Tournois structures. To match desired dispersion characteristics more closely, one can increase the number of cavities in the structure.

An analytical procedure for designing such coupled-cavity filters by use of a digital lattice technique has previously been established for both microwave filters^{36–38} and thin-film structures.^{22,39} We are particularly interested in the design of all-pass structures, i.e., structures with constant unity reflectance and wavelength-dependent phase properties. All-pass filters have been designed for temporal dispersion compensation.^{21,23} Here we will show with an example that the same technique can be used to design structures with spatial dispersion. Our goal is again to design a structure exhibiting a linear spatial shift along the x direction with wavelength. The example structure consists of five reflectors with four cavities in between. The last reflector has unity reflectance. Thus the reflectance of the structure is 100%, neglecting any absorption. In the first stage of the design, all cavity lengths are assumed to be equal with a cavity round-trip time T . The transfer function of an all-pass filter with N cavities is then given by Eq. (15), where $z^{-1} = \exp(-j\omega T)$. $A_N^R(z)$ is the reverse polynomial of $A_N(z)$ of order N :

$$H_{\text{AP}}(z) = z^{-N} \frac{1 + \sum_{n=1}^N a_n z^n}{1 + \sum_{n=1}^N a_n z^{-n}} = \frac{A_N^R(z)}{A_N(z)}. \quad (15)$$

In the first step of the design process, a polynomial $A_N(z)$ is determined such that the phase of $H_{\text{AP}}(z)$ approximates the shape of the desired phase response.^{23,40,41} The resulting transfer function $H_{\text{AP}}(z)$ exhibits a periodic behavior with the period given by the free spectral range $\text{FSR} = 1/T$.²² The expected shift can be calculated by the choice of a cavity round-trip time and a propagation angle in the cavity. Figure 7 shows the influence of the optical thickness of the cavity on the expected spatial shift with wavelength. The shape of the dispersion is the same for all three cavity lengths. The total shift increases proportionally with the cavity length, while at the same time the operating range decreases inversely with the length. Thus the dispersion is proportional to the square of the cavity length.

After choosing an appropriate cavity length to obtain the desired dispersion, we need to realize the partial reflectors as thin-film structures. The reflection coefficients r_i ($i = 1$ to 4, $r_5 = 1$) of the reflectors are deduced by use of an order-reduction technique. Starting with order $m = N$, we reduce the order m of the polynomial $A_m(z)$ in each step by 1. The coeffi-

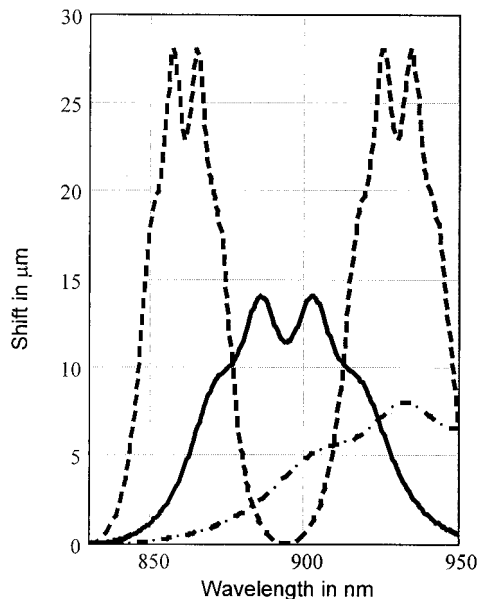


Fig. 7. Expected shift for a four-cavity structure is plotted as a function of wavelength for three different cavity optical thicknesses (dash-dotted curve, $L_c = 1.7 \mu\text{m}$; solid curve, $L_c = 2.9 \mu\text{m}$; dashed curve, $L_c = 5.8 \mu\text{m}$). The same transfer function $H_{AP}(z)$ is used for all calculations, and a group-propagation angle of 20° is assumed in the cavity.

coefficients of the polynomial $A_m(z)$ are $a_{m,\text{index}}$. The algorithm is given in Eqs. (16) and (17)⁴²:

$$r_{N+1-m} = -a_{m,m}, \quad (16)$$

$$A_{m-1}(z) = \frac{A_m(z) - a_{m,m}A_m(z^{-1})z^{-m}}{1 - a_{m,m}^2}. \quad (17)$$

Once the necessary reflection coefficients are determined, the reflectors can be designed with standard thin-film design procedures. Another approach is to approximate the reflectors by available quarter-wave structures and correct for the error in the reflectivity by modification of the individual cavity lengths.²³ After the reflectors are designed, it is important to subtract the optical thickness of each reflector from the corresponding optical cavity length because the reflector constitutes part of the round-trip time. The necessity to implement the reflector within the optical thickness of the cavity sets a lower limit on the cavity thickness and thus on the maximum achievable operating wavelength range. However, the cavity length cannot be chosen too large, as field interference is necessary for the operation of the device. If the distances between the reflectors are too large, a pulse is split into several pulses, and an optical rattle is obtained.⁴³

For our four-cavity example, we choose an optical cavity round-trip length of $5.8 \mu\text{m}$, Ta_2O_5 as the cavity material, s-polarized light, and an incidence angle of 54° . This corresponds to a physical thickness of $2.6 \mu\text{m}$ for each cavity. After the reflectors are designed, the resulting SiO_2 - Ta_2O_5 thin-film structure has 33 layers and a total thickness of $15.4 \mu\text{m}$. In

Fig. 8(a) the physical layer thicknesses are graphed. The composition of this structure is given in Appendix D. Figure 8(b) plots the resulting shift as a function of wavelength for this structure. A linear shift is obtained over a narrow wavelength range, demonstrating that this technique permits the design of narrowband structures with high dispersion. In Fig. 8(c) the E-field amplitudes parallel to the interface of the forward-propagating wave are plotted as a function of the position in the structure. For longer wavelengths a larger amount of energy buildup occurs in the structure. As discussed for the single-cavity resonators, this wavelength-dependent energy storage causes spatial and temporal dispersion. We also see that, for a structure with more than one cavity, part of the dispersion can be attributed to a wavelength-dependent penetration depth.

In conclusion, we demonstrated in this section that coupled-cavity all-pass filters can be designed to exhibit linear spatial dispersion using a digital lattice filter technique. Furthermore, the technique can be employed to design structures with a nonmonotonic shift as a function of wavelength. The major practical limitation we found in this approach is the necessity to design reflectors with very low reflectivity if a larger number of cavities is desired. For example, a linear eight-cavity design calls for five reflectors with less than 10% reflectivity, of which three should have less than 2% reflectivity. Therefore it becomes quite difficult to design appropriate thin-film reflectors for structures with a higher number of cavities. As the only way to achieve a larger free spectral range without decreasing the total spatial shift is to decrease the cavity length and thus increase the number of cavities, this technique is, in practice, limited to the design of narrowband structures. Again, this is a limitation of this specific design technique; by use of a different design technique, structures with dispersion over a broad wavelength range can be designed as discussed in Section 4. Only a subset of all possible structures is considered in this section—structures with large cavities separated by reflectors.

6. Structures That Employ a Combination of Wavelength-Dependent Penetration Depth and Stored Energy

In Sections 4 and 5 we discussed two methods for designing the dispersion characteristics of thin-film structures. Each method applies to a subset of all possible structures—the method in Section 4 applies to double-chirped structures and that in Section 5 applies to coupled-cavity structures. Although the periodic structures in Section 2 do not have enough degrees of freedom to allow for the design of a linear spatial shift as a function of wavelength, both of these methods have a sufficient number of degrees of freedom to obtain a linear shift at least within a certain wavelength range. In this section we investigate how a thin-film structure can be designed without limiting the degrees of freedom by just considering a specific type of structure. For fabrication purposes it normally does not matter if the structure is double

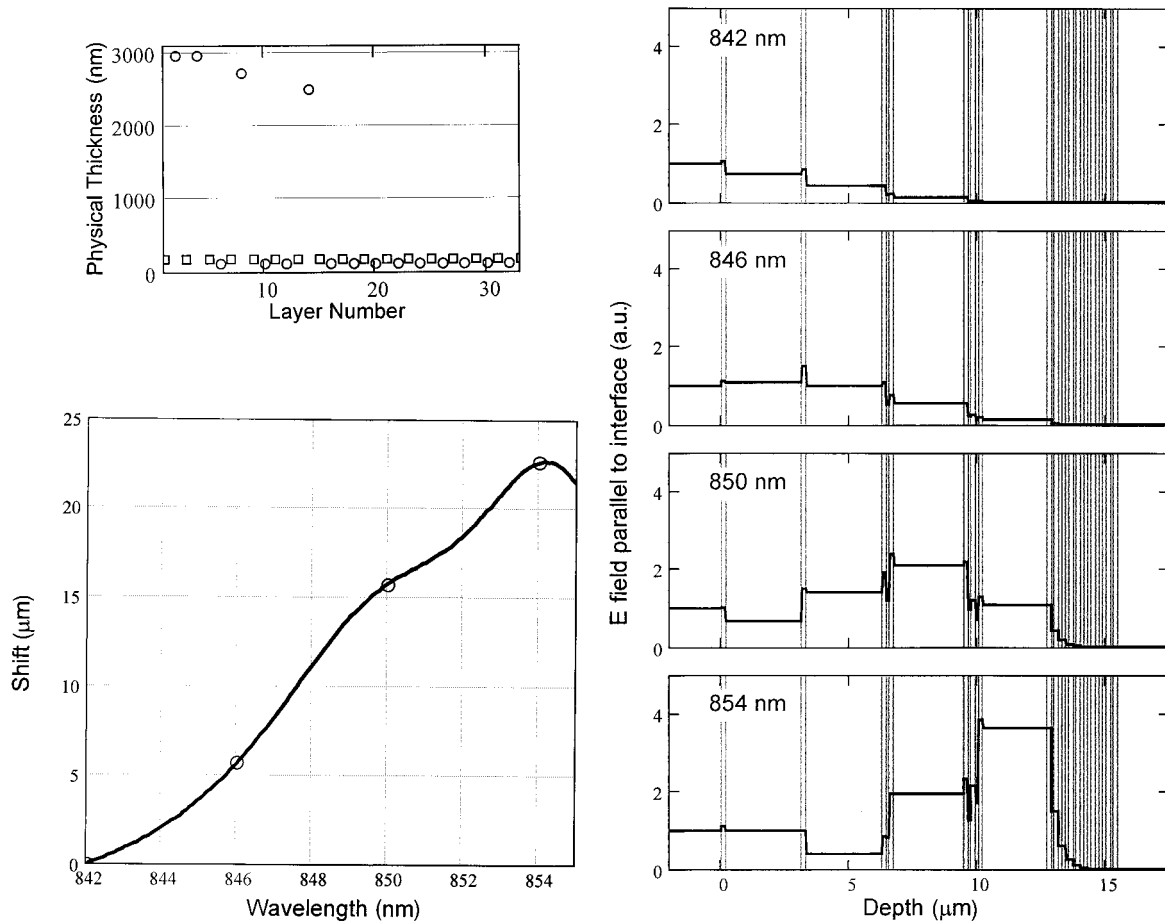


Fig. 8. (a) Physical layer thicknesses for a 33-layer $\text{SiO}_2\text{-Ta}_2\text{O}_5$ four-cavity structure (SiO_2 data, squares; Ta_2O_5 data, circles). (b) Theoretically calculated shift as a function of wavelength structure at a 54° incidence angle and s polarization. The reflectance of the structure is 100%. (c) E fields parallel to the interfaces of the forward-propagating waves as a function of the position in the structure for four wavelengths—842, 846, 850, and 854 nm. The vertical lines indicate the position of the interfaces between layers. Light is incident from the left, and the structure extends from 0 to $15.4\ \mu\text{m}$. For longer wavelengths a larger amount of energy buildup occurs in the structure. This causes spatial and temporal dispersion. We also see that part of the dispersion can be attributed to a wavelength-dependent penetration depth.

chirped, coupled cavity, or something completely different. More likely, the total thickness of the structure, the minimum and maximum thicknesses of individual layers, and the choice of materials set the limits to what can be fabricated. Therefore we would ideally investigate all possible structures that can be fabricated and find the one that most closely matches our desired dispersion characteristics. Unfortunately, the computation time of this approach becomes prohibitive for more than a couple of layers. This is a common problem in the design of thin-film filters with specified reflectance and transmittance characteristics.^{24–29} Here we explore how numerical techniques developed for the design of thin-film filters can be applied to the design of thin-film structures with spatial dispersion.

The design of thin-film filters is normally divided into two steps. In the first step, a start design is synthesized that approximately fulfills the required characteristics.²⁸ In the second step, numerical optimization procedures are used to gradually improve

the performance of the start design.²⁹ The performance of a design is measured by a merit function MF—a single number comparing the current design characteristics with the desired design characteristics.⁴⁴ The definition of the merit function we use is given in Eq. (18), where Q_i is the current value of a quantity of interest, Q_i^T is the target value of that quantity, ΔQ_i is the acceptable deviation, N is the number of sampling points, and p is the norm used:

$$\text{MF} = \left(\frac{1}{N} \sum_{i=1}^N \left| \frac{Q_i^T - Q_i}{\Delta Q_i} \right|^p \right)^{1/p}. \quad (18)$$

In the case of $p = 2$, the merit function is, e.g., the root-mean-square difference between the current values and the target values of the quantities of interest.

The calculation of the merit function is by no means limited to reflectance or transmittance values. In the same manner, we can specify a desired spatial shift as a function of wavelength and judge the performance of the current design by sampling the shift

at different wavelengths. Therefore the same numerical refinement techniques used to design thin-film filters can be applied to the design of thin-film structures with spatial dispersion. Any one of the analytical methods discussed in Sections 2, 4, and 5 can be used to generate a starting design. In our experience, the most important property of the starting design is the elimination of strong ripple, i.e., provision of impedance matching. Rapid oscillations in the shift with wavelength are difficult to remove by numerical optimization. We had more success in starting with a low but constant dispersion and increasing it during optimization. To ensure a constant dispersion, we normally calculate the merit function by employing a p norm with p between 6 and 10. This large p norm ensures an approximately identical error in the shift for all wavelengths.⁴⁵ Thus the resulting shift is, e.g., linear but offset from the originally specified shift. The sampling points have to be chosen close enough in wavelength to prevent oscillations between the points. A spacing of around 2 nm at 850 nm appears to work well.

We implemented six numerical optimization techniques—golden-section search,⁴⁵ secant method,⁴⁵ conjugate-gradient algorithm,⁴⁵ Broyden–Fletcher–Goldfarb–Shanno,⁴⁵ damped least-squares method,²⁹ and Hooke and Jeeves pattern search.⁴⁶ The first two methods are one-dimensional search methods; i.e., the different parameters are optimized sequentially. The other methods vary all parameters simultaneously. All methods search for the local minimum of the merit function. A lower nonlocal optimum may be found, though, by e.g., one choosing a large interval size of the golden-section search or by taking large steps in the Hooke and Jeeves pattern search technique. Our design algorithm uses the different numerical optimization techniques sequentially. This is successful, as a different design method may find a lower minimum if one method is stuck in a shallow local optimum. Numerical optimization allows the design of structures with dispersion characteristics that cannot be achieved by use of the analytical techniques discussed in the previous sections.

As an example, we designed a 66-layer, 13.4- μm -thick, thin-film structure with a linear shift over a 20-nm wavelength range around 830 nm. This type of medium-wide wavelength range is difficult to achieve with the double-chirped structures in Section 4 or the coupled-cavity structures in Section 5. We used an impedance-matched Bragg stack as the start design. We refined the design, specifying a linearly increasing spatial shift for 20 different wavelengths. The start structure had a reflectivity of 100%. To keep the reflectivity high, we used a gold coating as the last layer. To prevent loss, we could also specify the last layers of the structure as a Bragg stack. In our design algorithm we can set which layers are to be changed and what the minimum and maximum layer thicknesses are. This guarantees that the design can be fabricated. In the final design the minimum layer thickness is 57 nm, and the maximum

thickness is 454 nm. The composition of this structure is given in Appendix D. In Fig. 9(a) the physical layer thicknesses are plotted. Figure 9(b) shows the shift as a function of wavelength for the designed 66-layer structure. A highly linear shift is obtained. To investigate the origins of the observed dispersion, we plotted in Fig. 9(c) the E fields parallel to the interfaces as function of the position in the stack for four wavelengths. We see that the penetration depth increases for longer wavelengths and more energy is stored at the same time. Thus this general structure relies on a combination of these two types of dispersion.

To verify the validity of these dispersion concepts, we experimentally tested the 66-layer $\text{SiO}_2\text{-Ta}_2\text{O}_5$ structure discussed in Fig. 9. The experiment is again conducted with the setup depicted in Fig. 3. In contrast to the experiment discussed in Section 2, only one beam exits the structure, which demonstrates the successful suppression of all other reflections by impedance matching. To obtain the center position of the beams, we fitted the experimental data to a Gaussian beam profile. Figure 10 plots the resulting shift of the beam center as a function of wavelength (circles). The theoretical shift is calculated with a plane-wave approximation and the transfer-matrix method (solid curve). The linear shift between 820 and 840 nm is clearly visible. As the shift does not exhibit any rapid changes in this wavelength range, the plane-wave approximation predicts the experimentally observed shift accurately. The rise and fall in the shift for wavelengths larger than 840 nm explains why the plane-wave approximation is not as accurate in this regime. The slight difference between the shifts in Figs. 9(b) and 10 is due to the fact that the first calculation includes the back-side gold coating and the second does not. The overall excellent agreement between the experimentally observed shift and the theoretically expected shift confirms the above-discussed concepts for obtaining spatial dispersion.

7. Conclusion

In this treatment we discussed four ways of designing structures with high spatial dispersion. In Section 2 we demonstrated the strong spatial dispersion of periodic thin-film structures close to the stop-band edge both in theory and in experiment. Unfortunately, periodic structures with two layers per period do not offer enough degrees of freedom for the design of structures with desired dispersion characteristics, e.g., a linear shift with wavelength. One way to overcome this limitation is to increase the number of layers per period. This method should be used if a structure with constant effective properties is desired. Here, however, we were more interested in the aggregate transfer function from entering to exiting the structure. That is, we wanted to design a structure exhibiting a spatial beam shift along the exit surface with wavelength. In that case, it does not matter what happened to the beam within the structure. Taking this into account, we are no

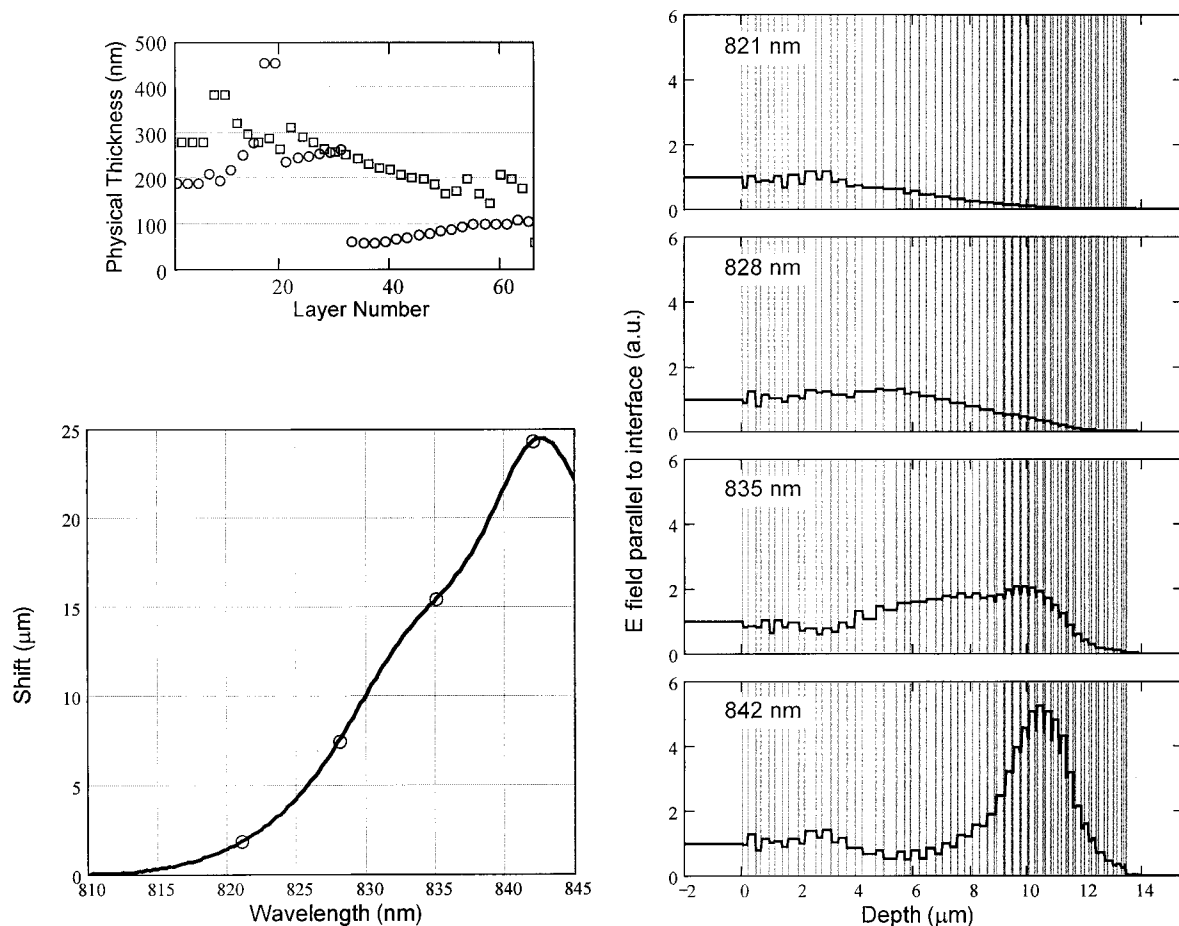


Fig. 9. (a) Physical layer thicknesses for a 66-layer, numerically optimized $\text{SiO}_2\text{-Ta}_2\text{O}_5$ structure (SiO_2 data, squares; Ta_2O_5 data, circles). (b) Theoretically calculated shift as a function of wavelength structure at a 54° incidence angle and p polarization. The reflectance of the structure is improved to nearly 100% by a gold layer on the extreme right. (c) E fields parallel to the interfaces of the forward-propagating waves as a function of the position in the structure for four wavelengths—821, 828, 835, and 842 nm. The vertical lines indicate the position of the interfaces between layers. Light is incident from the left, and the structure extends from 0 to $13.4\ \mu\text{m}$. We see that the dispersion is due to both a wavelength-dependent penetration depth and a wavelength-dependent amount of stored energy.

longer limited to periodic structures. Considering that spatial and temporal dispersion are approximately proportional, we modified methods used for temporal dispersion compensation to obtain spatial dispersion. In Section 4 we showed that the wavelength-dependent penetration depth of double-chirped structures can be used to obtain spatial dispersion and that these structures are particularly useful for broadband designs. In that section we also found that nonresonant energy storage makes an important contribution to the shift and that the obtained shift cannot be explained from pure geometrical reasoning. The coupled-cavity structures discussed in Section 5 employ a wavelength-dependent amount of stored energy to obtain dispersion and are effective for narrowband designs. Finally, in Section 6 we demonstrated in theory and experiment that structures that use a combination of a wavelength-dependent turning point and stored energy can be designed using numerical optimization methods.

Figure 11 compares the results obtained for the

periodic structure from Section 2 and the nonperiodic structure from Section 6. The results are scaled to the 1550-nm wavelength range for better comparison with current commercial interests for telecommunication. The total amount of shift can be significantly increased by one performing multiple passes through the structure as discussed in Ref. 9. Figure 11 graphs the shift after one bounce and after eight bounces. Eight bounces are well possible, as we have demonstrated in Ref. 47. The nonperiodic structure exhibits a total shift comparable with that of the periodic structure. But the same shift is obtained with just a third of layers, and the observed shift is linear with wavelength, which is much more desirable for practical applications. Furthermore, the nonperiodic structure is essentially lossless as all loss reflections (e.g., front-surface reflection) are suppressed. This shows the great potential of nonperiodic structures as compact dispersive devices.

Thin-film structures with high spatial dispersion are interesting as compact multiplexing and demultiplexing devices, which separate beams of different

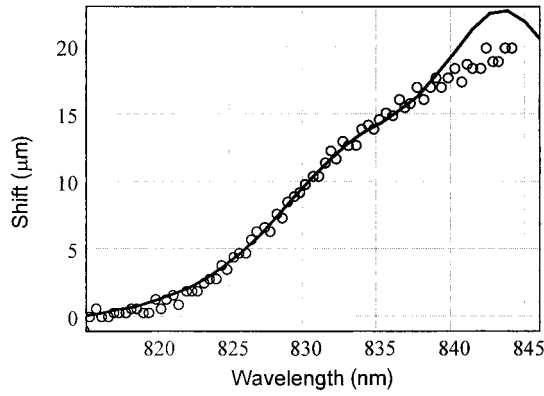


Fig. 10. Experimentally observed spatial dispersion of a 66-layer $\text{SiO}_2\text{-Ta}_2\text{O}_5$ dielectric stack with a total thickness of $13.4\text{ }\mu\text{m}$ on a quartz substrate for an incidence angle of 54° and p polarization. The experimental shift of the peak (circles) as a function of wavelength shows excellent agreement with the theoretical calculation (solid curve).

wavelengths by spatial beam shifting.⁹ The spatial dispersion could also be converted into an angular dispersion by a lens in sequence with the structure. Therefore the device could be used for wavelength-dependent beam steering. Future integrated photonic systems might use the discussed concepts to obtain spatial dispersion. Furthermore, the ideas considered here for one-dimensional thin-film structures can be transferred to two- or three-dimensional structures. Two-dimensional photonic crystal structures fabricated by lithography, for example, are by no means limited to periodic structures. As seen here for one-dimensional structures, breaking the periodicity actually offers more design freedom and interesting new physics. The difficult task is to design

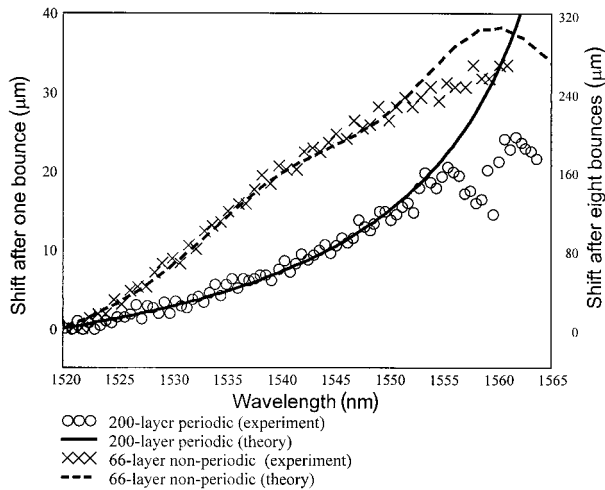


Fig. 11. Comparison of the results for the 200-layer periodic structure in Section 2 and the 66-layer nonperiodic structure in Section 6. The results are scaled to the 1550-nm wavelength range for better comparison [circles, 200-layer periodic (experiment); solid curve, 200-layer periodic (theory); exes, 66-layer non-periodic (experiment); dashed curve, 66-layer nonperiodic (theory)].

two- or three-dimensional structures with the desired characteristics. The coupled-cavity structures designed by digital lattice techniques could be a good starting point, as coupled-cavities in more dimensions have been investigated previously for microwave filters.^{36–38}

Appendix A: Bloch Dispersion Relation

For an infinite periodic medium with two layers per period, the dispersion relation is given by Eq. (A1).³⁰ In this equation, K is the amplitude of the wave vector in the z direction of the periodicity, β is the amplitude of the wave vector parallel to the layers in the x direction, n_a and n_b are the refractive indices, and l_a and l_b are the layer thicknesses of the two different materials:

$$\begin{aligned} \cos[K(l_a + l_b)] = & \cos\left\{\left[\left(\frac{\omega}{c}n_a\right)^2 - \beta^2\right]^{1/2}l_a\right\} \\ & \times \cos\left\{\left[\left(\frac{\omega}{c}n_b\right)^2 - \beta^2\right]^{1/2}l_b\right\} \\ & - \Delta(\beta, \omega)\sin\left\{\left[\left(\frac{\omega}{c}n_a\right)^2 - \beta^2\right]^{1/2}l_a\right\} \\ & \times \sin\left\{\left[\left(\frac{\omega}{c}n_b\right)^2 - \beta^2\right]^{1/2}l_b\right\}. \quad (\text{A1}) \end{aligned}$$

$\Delta(\beta, \omega)$ is given by Eq. (A2) for TE polarization and by Eq. (A3) for TM polarization:

$$\Delta_{\text{TE}}(\beta, \omega) = \frac{1}{2} \left\{ \frac{\left[\left(\frac{\omega}{c}n_b\right)^2 - \beta^2\right]^{1/2}}{\left[\left(\frac{\omega}{c}n_a\right)^2 - \beta^2\right]^{1/2}} + \frac{\left[\left(\frac{\omega}{c}n_a\right)^2 - \beta^2\right]^{1/2}}{\left[\left(\frac{\omega}{c}n_b\right)^2 - \beta^2\right]^{1/2}} \right\}, \quad (\text{A2})$$

$$\begin{aligned} \Delta_{\text{TM}}(\beta, \omega) = & \frac{1}{2} \left\{ \frac{n_a^2 \left[\left(\frac{\omega}{c}n_b\right)^2 - \beta^2\right]^{1/2}}{n_b^2 \left[\left(\frac{\omega}{c}n_a\right)^2 - \beta^2\right]^{1/2}} \right. \\ & \left. + \frac{n_b^2 \left[\left(\frac{\omega}{c}n_a\right)^2 - \beta^2\right]^{1/2}}{n_a^2 \left[\left(\frac{\omega}{c}n_b\right)^2 - \beta^2\right]^{1/2}} \right\}. \quad (\text{A3}) \end{aligned}$$

This calculation can also be used to model the dispersion properties of a finite bulk periodic medium, neglecting all boundary effects.

Appendix B: Transfer-Matrix Dispersion Relation

For nonperiodic dielectric stacks the relations among the incident, the transmitted, and the reflected fields can be obtained by use of a standard transfer-matrix

method. Assuming that no light is incident from the right side onto the stack and that the transmitted field has unity magnitude, the incident and reflected amplitudes on the left side of the stack can be calculated with Eq. (B1):

$$\begin{pmatrix} E_{\text{inc}} \\ E_{\text{refl}} \end{pmatrix} = \mathbf{D}_{0,1} \mathbf{P}_1 \mathbf{D}_{1,2} \mathbf{P}_2 \mathbf{D}_{2,3} \cdots \mathbf{P}_{N-1} \mathbf{D}_{N-1,N} \begin{pmatrix} 1 \\ 0 \end{pmatrix}. \quad (\text{B1})$$

Here the calculation is set up in terms of the E field parallel to the interfaces. The col(1, 0) vector on the right allows for some (unit) amplitude of field leaving the structure on the right but presumes no wave entering from the right. This is common practice in thin-film filter design, and the total field can easily be calculated from the field parallel to the boundary.²⁶ In Eq. (B1), \mathbf{P}_i and $\mathbf{D}_{i,i+1}$ are the propagation and interface matrices obtained from Maxwell's equations. $\mathbf{P}_i(\beta, \omega)$ is given in Eq. (B2), where n_i is the refractive index of layer i , d_i is the layer thickness, and c is the speed of light in vacuum:

$$\mathbf{P}_i(\beta, \omega) = \begin{bmatrix} \exp\left\{i\left[\left(\frac{\omega}{c} n_i\right)^2 - \beta^2\right]^{1/2} d_i\right\} & 0 \\ 0 & \exp\left\{-i\left[\left(\frac{\omega}{c} n_i\right)^2 - \beta^2\right]^{1/2} d_i\right\} \end{bmatrix}. \quad (\text{B2})$$

The interface matrices $\mathbf{D}_{i,i+1}(\beta, \omega)$ given in Eq. (B3) depend on the reflection coefficients $r_{i,i+1}(\beta, \omega)$ and the transmission coefficients $t_{i,i+1}(\beta, \omega)$ between adjacent layers that are given by Eqs. (B4) and (B5):

$$\mathbf{D}_{i,i+1}(\beta, \omega) = \frac{1}{t_{i,i+1}(\beta, \omega)} \begin{bmatrix} 1 & r_{i,i+1}(\beta, \omega) \\ r_{i,i+1}(\beta, \omega) & 1 \end{bmatrix}, \quad (\text{B3})$$

$$r_{i,i+1}(\beta, \omega) = \frac{n_{\text{eff},i}(\beta, \omega) - n_{\text{eff},i+1}(\beta, \omega)}{n_{\text{eff},i}(\beta, \omega) + n_{\text{eff},i+1}(\beta, \omega)}, \quad (\text{B4})$$

$$t_{i,i+1}(\beta, \omega) = \frac{2n_{\text{eff},i}(\beta, \omega)}{n_{\text{eff},i}(\beta, \omega) + n_{\text{eff},i+1}(\beta, \omega)}. \quad (\text{B5})$$

The effective refractive indices for the cases of TE and TM polarizations are given by Eqs. (B6) and (B7), respectively.²⁶ If the expression under the square root becomes negative as, e.g., in the case of total internal reflection, the sign of the effective refractive indices has to be chosen carefully to prevent unphysical exponentially growing field amplitudes, though the method does then model such situations correctly:

$$n_{\text{eff,TE},i}(\beta, \omega) = n_i \left[1 - \left(\frac{c\beta}{\omega n_i} \right)^2 \right]^{1/2}, \quad (\text{B6})$$

$$n_{\text{eff,TM},i}(\beta, \omega) = \frac{n_i}{\left[1 - \left(\frac{c\beta}{\omega n_i} \right)^2 \right]^{1/2}}. \quad (\text{B7})$$

Once the incident and reflected fields, E_{inc} and E_{refl} , are obtained from Eq. (B1), the phase change upon reflection can be calculated with (B8):

$$\phi_{\text{refl}}(\beta, \omega) = \arg[E_{\text{refl}}(\beta, \omega)] - \arg[E_{\text{inc}}(\beta, \omega)]. \quad (\text{B8})$$

Assuming a total stack thickness L , the wave vector $K(\beta, \omega)$ in the z direction is related to the phase change upon reflection as given in Eq. (B9):

$$K(\beta, \omega) = \frac{\phi_{\text{refl}}(\beta, \omega)}{2L}. \quad (\text{B9})$$

Appendix C: Approximate Calculation of $\delta\beta/\delta\omega$

Here we calculate $\partial\beta/\partial\omega$ under the assumption that the interface matrices $\mathbf{D}_{i,i+1}$ in Eq. (B3) can be ap-

proximated by unity matrices. This approximation is justified if the reflection of the interfaces between layers is small. As shown in Ref. 18, WKB-type approximations can also be used for a wider class of structures. In this case the phase change upon reflection is solely caused by the propagation matrices \mathbf{P}_i . The approximated phase upon reflection ϕ_{appr} is then given by expression (C1):

$$\phi_{\text{appr}}(\beta, \omega) \approx -2 \sum_i \left\{ \left[\left(\frac{\omega}{c} n_i \right)^2 - \beta^2 \right]^{1/2} d_i \right\}. \quad (\text{C1})$$

Thus the derivatives of the approximate dispersion relation with respect to ω and β are expressions (C2) and (C3):

$$\left. \frac{\partial\phi_{\text{appr}}(\beta, \omega)}{\partial\omega} \right|_{\beta=\text{const}} \approx 2 \sum_i \left\{ \frac{\frac{n_i^2}{c} d_i}{\left[n_i^2 - \left(\frac{\beta c}{\omega} \right)^2 \right]^{1/2}} \right\}, \quad (\text{C2})$$

$$\left. \frac{\partial\phi_{\text{appr}}(\beta, \omega)}{\partial\beta} \right|_{\omega=\text{const}} \approx -2 \sum_i \left\{ \frac{\frac{\beta c}{\omega} d_i}{\left[n_i^2 - \left(\frac{\beta c}{\omega} \right)^2 \right]^{1/2}} \right\}. \quad (\text{C3})$$

Using the rules for taking implicit derivatives, we get the expression for $\partial\beta/\partial\omega$ given in expression (C4):

$$\left(\frac{\partial\beta}{\partial\omega}\right)_{\text{appr}} \bigg|_{K=\text{const}} = \frac{-\partial\phi_{\text{appr}}/\partial\omega}{\partial\phi_{\text{appr}}/\partial\beta} \approx \frac{\omega}{\beta c^2} \frac{\sum_i \left\{ n_i^2 d_i / \left[n_i^2 - \left(\frac{\beta c}{\omega} \right)^2 \right]^{1/2} \right\}}{\sum_i \left\{ d_i / \left[n_i^2 - \left(\frac{\beta c}{\omega} \right)^2 \right]^{1/2} \right\}}. \quad (\text{C4})$$

Substituting $\beta = \omega/c \sin(\theta)$, where θ is the incidence angle in vacuum, we can rewrite expression (C4) as expression (C5):

$$\left(\frac{\partial\beta}{\partial\omega}\right)_{\text{appr}} \bigg|_{K=\text{const}} \approx \frac{1}{c \sin(\theta)} \frac{\sum_i \{ n_i^2 d_i / [n_i^2 - \sin^2(\theta)]^{1/2} \}}{\sum_i \{ d_i / [n_i^2 - \sin^2(\theta)]^{1/2} \}}. \quad (\text{C5})$$

We see that the resulting approximate expression for $\partial\beta/\partial\omega$ depends only on the incident angle and not on the frequency. Thus $\partial\beta/\partial\omega$ is independent of frequency within this approximation. We found numerically that $\partial\beta/\partial\omega$ is approximately constant for all the structures with linear dispersion that we tested. Furthermore, expression (C5) can be used to calculate the correct constant to within a 20% error. A more rigorous proof of this property still needs to be performed.

Appendix D: Composition of the Designs Discussed in Sections 5 and 6

		Section			
		5	6	Section 6	
Substrate Material	Layer Number	Physical Thickness (nm)	Layer Number	Physical Thickness (nm)	
Ta ₂ O ₅	1	188.0	35	58.0	
SiO ₂	2	168.3	36	228.8	
Ta ₂ O ₅	3	2954.0	37	57.0	
SiO ₂	4	168.3	38	221.5	
Ta ₂ O ₅	5	2967.0	39	61.0	
SiO ₂	6	168.3	40	219.4	
Ta ₂ O ₅	7	118.9	41	66.0	
SiO ₂	8	168.3	42	207.0	
Ta ₂ O ₅	9	2728.0	43	70.0	
SiO ₂	10	168.3	44	199.7	
Ta ₂ O ₅	11	118.9	45	75.0	
SiO ₂	12	168.3	46	198.6	
Ta ₂ O ₅	13	118.9	47	80.0	
SiO ₂	14	168.3	48	185.1	
Ta ₂ O ₅	15	2495.0	49	84.0	
SiO ₂	16	168.3	50	163.3	

		Section			
		5	6	Section 6	
Substrate Material	Layer Number	Physical Thickness (nm)	Layer Number	Physical Thickness (nm)	
Ta ₂ O ₅	17	118.9	453.0	51	89.0
SiO ₂	18	168.3	286.0	52	171.6
Ta ₂ O ₅	19	118.9	453.0	53	93.0
SiO ₂	20	168.3	263.1	54	196.0
Ta ₂ O ₅	21	118.9	235.0	55	98.0
SiO ₂	22	168.3	311.0	56	164.3
Ta ₂ O ₅	23	118.9	245.0	57	98.0
SiO ₂	24	168.3	289.1	58	144.6
Ta ₂ O ₅	25	118.9	249.0	59	98.0
SiO ₂	26	168.3	276.6	60	205.9
Ta ₂ O ₅	27	118.9	254.0	61	98.0
SiO ₂	28	168.3	262.1	62	197.6
Ta ₂ O ₅	29	118.9	258.0	63	109.0
SiO ₂	30	168.3	257.9	64	175.8
Ta ₂ O ₅	31	118.9	263.0	65	104.0
SiO ₂	32	168.3	251.7	66	57.2
Ta ₂ O ₅	33	118.9	60.0		
SiO ₂	34	168.3	241.3		

Many thanks to A. Clark, A. Zheng, and P. J. Anthony of JDS Uniphase for the fabrication of the thin-film structures. M. Gerken thanks F. X. Kärtner for giving her the opportunity to spend the summer of 2001 in his research group at the University of Karlsruhe in Germany. M. Gerken also acknowledges support of the Sequoia Capital Stanford Graduate Fellowship. This research was supported by the University of New Mexico under subcontract 3-17271-7810 and the Defense Advanced Research Projects Agency grant MDA972-00-1-0024.

References

1. E. Hecht, *Optik* (Addison-Wesley, Bonn, Germany, 1989).
2. R. Zengerle, "Light propagation in singly and doubly periodic planar waveguides," *J. Mod. Opt.* **34**, 1589–1617 (1987).
3. J. P. Dowling and C. M. Bowden, "Anomalous index of refraction in photonic bandgap materials," *J. Mod. Opt.* **41**, 345–351 (1994).
4. S.-Y. Lin, V. M. Hietala, L. Wang, and E. D. Jones, "Highly dispersive photonic band-gap prism," *Opt. Lett.* **21**, 1771–1773 (1996).
5. H. Kosaka, T. Kawashima, A. Tomita, M. Notomi, T. Tamamura, T. Sato, and S. Kawakami, "Superprism phenomena in photonic crystals," *Phys. Rev. B* **58**, R10096–R10099 (1998).
6. S. Enoch, G. Tayeb, and D. Maystre, "Numerical evidence of ultrarefractive optics in photonic crystals," *Opt. Commun.* **161**, 171–176 (1999).
7. H. Kosaka, T. Kawashima, A. Tomita, M. Notomi, T. Tamamura, T. Sato, and S. Kawakami, "Superprism phenomena in photonic crystals: toward microscale lightwave circuits," *J. Lightwave Technol.* **17**, 2032–2038 (1999).
8. B. Gralak, S. Enoch, and G. Tayeb, "Anomalous refractive properties of photonic crystals," *J. Opt. Soc. Am. A* **17**, 1012–1020 (2000).
9. B. E. Nelson, M. Gerken, D. A. B. Miller, R. Piestun, C.-C. Lin, and J. S. Harris, Jr., "Use of a dielectric stack as a one-dimensional photonic crystal for wavelength demultiplexing by beam shifting," *Opt. Lett.* **25**, 1502–1504 (2000).

10. E. Silvestre, J. M. Pottage, P. St. J. Russell, and P. J. Roberts, "Design of thin-film photonic crystal waveguides," *Appl. Phys. Lett.* **77**, 942–944 (2000).
11. A. N. Naumov, R. B. Miles, P. Barker, and A. M. Zheltikov, "Ultradispersive prisms and narrow-band tunable filters combining dispersion of atomic resonances and photonic band-gap structures," *Laser Phys.* **10**, 622–626 (2000).
12. M. Notomi, K. Yamada, A. Shinya, J. Takahashi, C. Takahashi, and I. Yokohama, "Extremely large group-velocity dispersion of line-defect waveguides in photonic crystal slabs," *Phys. Lett.* **87**, 253902-1–253902-4 (2001).
13. T. Ochiai and J. Sanchez-Dehesa, "Superprism effect in opal-based photonic crystals," *Phys. Rev. B* **64**, 245113-1–245113-7 (2001).
14. J. D. Joannopoulos, R. D. Meade, and J. N. Winn, *Photonic Crystals—Molding the Flow of Light* (Princeton U. Press, Princeton, N.J., 1995).
15. I. Walmsley, L. Waxer, and C. Dorrer, "The role of dispersion in ultrafast optics," *Rev. Sci. Instrum.* **72**, 1–29 (2001).
16. R. Szpöcs, K. Ferencz, C. Spielmann, and F. Krausz, "Chirped multilayer coatings for broadband dispersion control in femtosecond lasers," *Opt. Lett.* **19**, 201–203 (1994).
17. P. Tournois and P. Hartemann, "Bulk chirped Bragg reflectors for light pulse compression and expansion," *Opt. Commun.* **119**, 569–575 (1995).
18. N. Matuschek, F. X. Kärtner, and U. Keller, "Exact coupled-mode theories for multilayer interference coatings with arbitrary strong index modulations," *IEEE J. Quantum Electron.* **33**, 295–302 (1997).
19. N. Matuschek, F. X. Kärtner, and U. Keller, "Theory of double-chirped mirrors," *IEEE J. Sel. Top. Quantum Electron.* **4**, 197–208 (1998).
20. N. Matuschek, F. X. Kärtner, and U. Keller, "Analytical design of double-chirped mirrors with custom-tailored dispersion characteristics," *IEEE J. Quantum Electron.* **35**, 129–137 (1999).
21. G. Lenz and C. K. Madsen, "General optical all-pass filter structures for dispersion control in WDM systems," *J. Lightwave Technol.* **17**, 1248–1254 (1999).
22. C. K. Madsen and J. H. Zhao, *Optical Filter Design and Analysis—A Signal Processing Approach* (Wiley, New York, 1999).
23. M. Jablonski, Y. Takushima, and K. Kikuchi, "The realization of all-pass filters for third-order dispersion compensation in ultrafast optical fiber transmission systems," *J. Lightwave Technol.* **19**, 1194–1205 (2001).
24. P. Baumeister, "Design of multilayer filters by successive approximations," *J. Opt. Soc. Am.* **48**, 955–958 (1958).
25. J. A. Dobrowolski, "Completely automatic synthesis of optical thin film systems," *Appl. Opt.* **4**, 937–946 (1965).
26. H. A. MacLeod, *Thin-Film Optical Filters* (Institute of Physics Publishing, Philadelphia, Pa., 2001).
27. A. Thelen, *Design of Optical Interference Coatings* (McGraw-Hill, New York, 1989).
28. L. Li and J. A. Dobrowolski, "Computation speeds of different optical thin-film synthesis methods," *Appl. Opt.* **31**, 3790–3799 (1992), and references therein.
29. J. A. Dobrowolski and R. A. Kemp, "Refinement of optical multilayer systems with different optimization procedures," *Appl. Opt.* **29**, 2876–2893 (1990), and references therein.
30. A. Yariv and P. Yeh, "Electromagnetic propagation in periodic stratified media. II. Birefringence, phase matching, and x-ray lasers," *J. Opt. Soc. Am.* **67**, 438–448 (1977).
31. P. Yeh, A. Yariv, and C.-S. Hong, "Electromagnetic propagation in periodic stratified media. I. General theory," *J. Opt. Soc. Am.* **67**, 423–438 (1977).
32. J. W. Goodman, *Introduction to Fourier Optics* (McGraw-Hill, New York, 1996).
33. F. Oullette, "Dispersion cancellation using linearly chirped Bragg grating filters in optical waveguides," *Opt. Lett.* **12**, 847–849 (1987).
34. B. J. Eggleton, G. Lenz, N. Litchinitser, D. B. Patterson, and R. E. Slusher, "Implications of fiber grating dispersion for WDM communication systems," *IEEE Photon. Technol. Lett.* **9**, 1403–1405 (1997).
35. M. Sumetsky, B. J. Eggleton, and C. M. de Sterke, "Theory of group delay ripple generated by chirped fiber gratings," *Opt. Express* **10**, 332–340 (2002).
36. G. Matthaei, E. M. T. Jones, and L. Young, *Microwave Filters, Impedance-Matching Networks, and Coupling Structures* (Artech House, Norwood, Mass., 1980).
37. J. Hunter, *Theory and Design of Microwave Filters* (Institution of Electrical Engineers, London, 2001).
38. J.-S. Hong and M. J. Lancaster, *Microstrip Filters for RF/Microwave Applications* (Wiley-Interscience, New York, 2001).
39. E. M. Dowling and D. L. MacFarlane, "Lightwave lattice filters for optically multiplexed communication systems," *J. Lightwave Technol.* **12**, 471–486 (1994).
40. M. Lang and T. I. Laakso, "Simple and robust method for the design of allpass filters using least-squares phase error criterion," *IEEE Trans. Circuits Syst. II* **41**, 40–48 (1994).
41. K. Rajamani and Y.-S. Lai, "A novel method for designing allpass digital filters," *IEEE Signal Process Lett.* **6**, 207–209 (1999).
42. A. H. Gray, Jr. and J. D. Markel, "Digital lattice and ladder filter synthesis," *IEEE Trans. Audio Electroacoust.* **AU-21**, 491–500 (1973).
43. V. Narayan, E. M. Dowling, and D. L. MacFarlane, "Design of multimirror structures for high-frequency bursts and codes of ultrashort pulses," *IEEE J. Quantum Electron.* **30**, 1671–1680 (1994).
44. J. A. Dobrowolski, F. C. Ho, A. Belkind, and V. A. Koss, "Merit functions for more effective thin film calculations," *Appl. Opt.* **28**, 2824–2831 (1989).
45. E. K. P. Chong and S. H. Zak, *An Introduction to Optimization* (Wiley, New York, 1996).
46. T. E. Shoup and F. Mistree, *Optimization Methods with Applications for Personal Computers* (Prentice-Hall, Englewood Cliffs, N.J., 1987).
47. M. Gerken and D. A. B. Miller, "Thin-Film (DE)MUX based on group-velocity effects," in *Proceedings of the Twenty-Eighth European Conference on Optical Communication ECOC 2002*, P. Danielsen, ed. (ECOC, Copenhagen, Denmark, 2002), paper 11.3.3.